Available online at www.sciencedirect.com
SCIENCE DIRECT®
Pergamon
Acta Materialia 51 (2003) 2017–2030
Acta MATERIALIA
www.actamat-journals.com

On the propagation and coalescence of delamination cracks in compressed coatings: with application to thermal barrier systems

X. Chen [a,*], J.W. Hutchinson [a], M.Y. He [b], A.G. Evans [b]

[a] *Division of Engineering and Applied Sciences, Harvard University, 29 Oxford Street, Cambridge, MA 02138, USA*
[b] *Materials Department, University of California, Santa Barbara, CA 93106, USA*

Received 4 November 2002; received in revised form 11 December 2002; accepted 16 December 2002

Abstract

Coatings subject to residual compression eventually fail by buckle-driven delamination. The phenomenon is most vivid in thermal barrier coatings (TBCs) used in gas turbines. The failure evolution commences with the formation of a large number of small cracks at geometric imperfections near the interface. These cracks spread upon thermal exposure, particularly upon thermal cycling, because of the formation of a thermally grown oxide (TGO) beneath the TBC, which introduces normal and shear stress near the interface. Experimental observations indicate that some of these cracks coalesce to form large-scale delaminations susceptible to buckling. The mechanics governing crack coalescence and the consequent failure are addressed in the present analysis.

A model is introduced that simulates stresses induced in the TBC by spatial variations in TGO growth. Energy release rates for cracks evolving in this stress field are determined. Two related scenarios are considered, which differ in the way the TGO shape evolves. In both, contact between the crack faces and the consequent wedging action is responsible for ultimate coalescence. The wedging force induces a mode I stress intensity that becomes infinite as the cracks coalesce. The consequence is that, for some TGO shapes, the energy release rate is always non-zero, with a minimum at a characteristic crack length. This minimum establishes a criterion for crack coalescence and failure.

Based on these insights, finite element simulations have been used to predict cyclic crack growth rates in a TBC system that correlate well with experimental observations.

Keywords: Coalescence; Crack; Delamination; Thermal barrier coating; Toughness

1. Introduction

Multi-layer thermal barrier systems (Fig. 1) fail by the propagation and coalescence of micro-cracks within the outer layer of yttria stabilized zirconia (YSZ) [1–19]. The micro-cracks are motivated by localized tensile stresses in the thermal barrier that arise because of the strain misfit between the thermally grown oxide (TGO) and the other layers [4,6,8,9,11,12]. While the specifics are system dependent, there are commonalities (Fig. 1). The micro-cracks initiate at multiple sites,

* Corresponding author. Tel.: +1-617-4952891; fax: +1-617-4959837.
E-mail address: chen@esag.harvard.edu (X. Chen).

1359-6454/03/$30.00
doi:10.1016/S1359-6454(02)00620-1

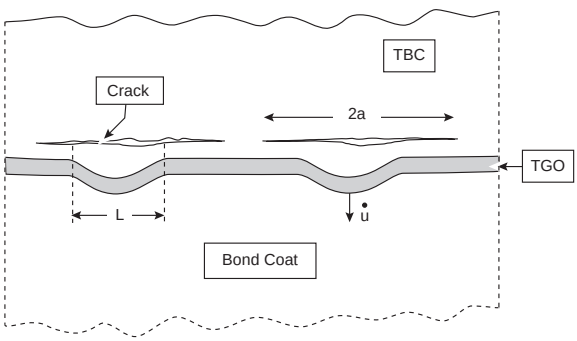

Fig. 1. A schematic of a crack configuration that arises in thermal barrier systems (see Fig. 2).

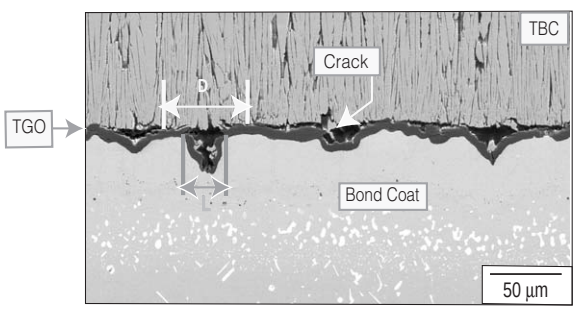

Fig. 2. A scanning electron image of a cross section of TBC system similar to Fig. 1 that has experienced 75% of its cyclic durability [9]. Note the undulations in the TGO and the cracks in the TBC just above the interface with the TGO.

either at or above the interface with the TGO [4,5,7,9,11,13]. They extend laterally from these sites as the system cycles. Eventually, a few adjacent micro-cracks coalesce into a crack large enough to exhibit large-scale buckling and spallation [4]. An example is illustrated in Figs. 1 and 2 [9]. In systems consisting of a Pt–aluminide bond coat and a columnar thermal barrier coating (TBC) made by electron beam physical vapor deposition (EB-PVD), the TGO exhibits a displacement instability directed into the bond coat. This displacement induces tensile stresses in the TBC above the instabilities (Figs. 1 and 2) [4–6,8–11], which cause cracks. Eventually, some of the cracks coalesce to cause failure.

In all cases, in the absence of cracks the TBC experiences an oscillating stress field with tension above the imperfections and compression outside. Accordingly, cracks that form have an energy release rate, G, that varies with micro-crack half-length, a, relative to imperfection wavelength, L. The objective is to determine the evolution of the energy release rate. Above the imperfection, where the stress is tensile, there is a rapid rise in G to a maximum [15]. This is followed by a decrease as the micro-crack front spreads into a region of compression and reverse shear. As neighboring cracks converge and coalesce, G attains a minimum, $G_{\min}$. As the system cycles, the thickness distribution of the TGO evolves and $G_{\min}$ increases. This increase is promoted by a wedging force that arises where the crack faces are in contact. The cracks coalesce and cause failure when $G_{\min}$ reaches the fracture toughness of the TBC, I_{tbc}, at the appropriate mode mixity. The challenge is to gain a fundamental understanding of $G_{\min}$ sufficient to ascertain its dependence on the stresses and dimensions. The intent of the present study is to establish basic mechanics principles governing crack coalescence and to apply these to problems of the type indicated in Fig. 1.

The problems reside within the broad mechanics category of cracks extending within oscillating residual stress fields [15,20,21]. The special feature is that the cracks are parallel to a free surface and consequently no net force acts across the putative crack plane. This unusual situation requires a careful analysis of the crack tip intensities because the minimum energy release rates as the cracks approach coalescence are small relative to the peak. Contact between portions of the crack faces, which arises as the cracks spread, plays an essential role. It promotes mode I behavior in a situation wherein, otherwise, the energy release rate would vanish as the cracks coalesce. The mechanics problem for generating the pre-cracking stresses is as follows. Matter is inserted along a plane parallel to the surface with a thickness distribution that enables the ensuing residual stress to vary in a periodic manner (Fig. 3). This approach for creating stress closely duplicates that experienced by thermal barrier systems, which may be attributed to the periodic displacements caused by growth of the TGO [4].

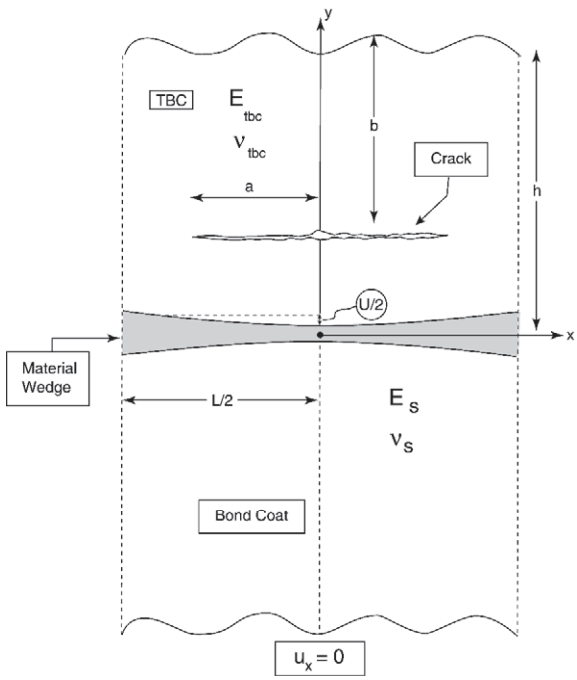

Fig. 3. The model used to examine the growth and coalescence of cracks represented in Fig. 1. The sinusoidal wedge simulates the spatially varying displacements associated with the TGO.

2. The stress field

The reduced plane strain problem is depicted in Fig. 3. A thin slab of material (effectively, the TGO) is wedged into the interface between the film (TBC with thickness h), and the substrate. The wedge has periodic thickness, with wavelength L. At the interface, $y = 0$, the displacement u_y induced by the wedge is discontinuous according to:

$$[u_y]^+_- \equiv u_y(y = 0 +) - u_y(y = 0-) = U_0 - U_1 \cos\frac{2\pi x}{L}, \tag{1}$$

where U_1 is a positive number representing the sinusoidal amplitude of the wedge. The uniform component, U_0, has no influence on the resulting stresses and plays no role in the present model since it displaces the TBC upward by a rigid body displacement. It is included to emphasize that the TGO thickens everywhere along its length. Only the oscillatory mass insertion contributes to the stresses, giving rise to a tensile stress σ_{yy} in the TBC at $x = 0$. Constrained lateral growth of the TGO produces lateral in-plane stress in the TGO which, in turn, gives rise to oscillating normal and shear stresses on the TGO/TBC interface when undulations arise [21]. The lateral growth stress is not considered in the present paper since the it is limited by plastic deformation of the TGO and thus the oscillatory interface stresses it produces will usually be small compared to the stresses due to wedging. The aim of this paper is to isolate the cracking mechanism of oscillatory stresses in combination with wedging contact. A more complete analysis would include the influence of the lateral growth stress in the TGO, but this would not change the essence of the mechanism. Across the interface, the tractions and the other displacement component u_x are continuous:

$$[\sigma_{yy}]^+_- = [\sigma_{xy}]^+_- = [u_x]^+_- = 0. \tag{2}$$

Attention is limited to a homogeneous, isotropic model to obtain representative analytical results: $E = E_{\rm tbc} = E_{\rm s}$ and $\nu = \nu_{\rm tbc} = \nu_{\rm s}$. The analysis can readily be extended to cases with elastic mismatch but the number of parameters multiplies rapidly. The traction boundary conditions are:

$$\sigma_{yy} = \sigma_{xy} = 0 \quad \text{at } y = h, \tag{3a}$$

and

$$\sigma_{yy} = \sigma_{xy} = 0 \quad \text{when } y \to -\infty. \tag{3b}$$

From Eq. (1), the airy stress functions for the TBC ($y \geq 0$) and the substrate ($y \leq 0$) can be taken as:

$$\begin{cases} \phi = f(y)\cos\dfrac{2\pi x}{L} & (y \leq 0), \\ \Phi = g(y)\cos\dfrac{2\pi x}{L} & (y \geq 0). \end{cases} \tag{4}$$

The stresses are related to the second derivatives of the airy stress functions:

$$\begin{aligned} &y \leq 0\text{: } \sigma_{xx} = \partial^2\phi/\partial y^2,\ \sigma_{yy} = \partial^2\phi/\partial x^2,\ \sigma_{xy} = -\partial^2\phi/\partial x\partial y, \\ &y \geq 0\text{: } \sigma_{xx} = \partial^2\Phi/\partial y^2,\ \sigma_{yy} = \partial^2\Phi/\partial x^2,\ \sigma_{xy} = -\partial^2\Phi/\partial x\partial y. \end{aligned} \tag{5}$$

Compatibility of the strains requires that [22]

$$\begin{cases} \nabla^4\phi = 0, & y \leq 0, \\ \nabla^4\Phi = 0, & y \geq 0. \end{cases} \tag{6}$$

The stress functions ϕ and Φ can be solved from the bi-harmonic differential equation (6) with boundary conditions (1)–(3). The stress components within the TBC at a distance b ($y = b-h$ with $b \leq h$) beneath the surface, caused by the wedge are:

$$\begin{cases} \sigma_{yy} = \dfrac{EU_1\pi \exp\left(-\dfrac{2\pi(b+h)}{L}\right)}{2L^3(1-\nu^2)} \\ [L^2(e^{4\pi b/L}-1)-2\pi L(b + b\, e^{4\pi b/L} + h - h\, e^{4\pi b/L})-8\pi^2 bh]\cos\dfrac{2\pi x}{L}, \\ \sigma_{xy} = \dfrac{EU_1\pi^2 \exp\left(-\dfrac{2\pi(b+h)}{L}\right)}{L^3(1-\nu^2)} \\ [Lh(e^{4\pi b/L}-1) + b(L-L\, e^{4\pi b/L} + 4\pi h)]\sin\dfrac{2\pi x}{L}. \end{cases} \tag{7}$$

If the TBC is very thick ($h \to \infty$), the stresses are:

$$\begin{cases} \sigma_{yy} = \dfrac{EU_1\pi}{2L^2(1-\nu^2)} e^{-2\pi y/L}(L + 2\pi y)\cos\dfrac{2\pi x}{L}, \\ \sigma_{xy} = \dfrac{EU_1\pi^2}{L^2(1-\nu^2)} e^{-2\pi y/L} y \sin\dfrac{2\pi x}{L}. \end{cases} \tag{8}$$

Eqs. (7) and (8) describe the stresses in TBC caused by the undulation and growth of the TGO. The normal and shear stresses are cosine and sinusoidal functions, respectively, multiplied by positive coefficients related to the geometric and elastic parameters.

The normal stress σ_{yy} is always the largest at the interface and decreases exponentially away from the interface. The shear stress σ_{xy} is zero at the interface and reaches maximum *inside* the TBC, at location b^*/L, given by the implicit relation:

$$\frac{h}{L} = \frac{1}{2\pi}\left[(e^{4\pi b^*/L}-1) + 2\pi\frac{b^*}{L}(e^{4\pi b^*/L} + 1)\right]\left[(e^{4\pi b^*/L}-1) + 4\pi\frac{b^*}{L}\right]^{-1}. \tag{9}$$

For thick films, $h \to \infty$, the maximum is located at, $y^*/L = 1/2\pi$. The presence of this maximum is important because it dictates the location where the mode II stress intensity factor reaches its largest value, discussed subsequently.

If the undulation wavelength of the wedge is $L/2$, with $[u_y]^+_- \equiv -U_2 \cos(4\pi x/L)$, then the stress field within an infinitely thick TBC layer is:

$$\begin{cases} \sigma_{yy} = \dfrac{EU_2\pi}{L^2(1-\nu^2)} e^{-4\pi y/L}(L + 4\pi y)\cos\dfrac{4\pi x}{L}, \\ \sigma_{xy} = \dfrac{EU_2\pi^2}{L^2(1-\nu^2)} e^{-4\pi y/L} 4y \sin\dfrac{4\pi x}{L}. \end{cases} \tag{10}$$

In the scenario discussed below, the evolution of the TGO shape with thermal cycling will be seen to be critical. The shape will be assumed to be roughly sinusoidal with wavelength L, in the early stages. As thermal cycling proceeds the undulations are observed to develop a dominant protrusion into the bond coat with a much smaller lobe pushing into the TBC, whereupon, the component of wavelength $L/2$ becomes increasingly prominent. At any stage, the TGO undulation is approximated by:

$$[u_y]^+_- = -U_1\left[\cos\frac{2\pi x}{L} + \Psi\cos\frac{4\pi x}{L}\right], \tag{11a}$$

where

$$\Psi = U_2/U_1. \tag{11b}$$

Ψ is a shape factor that gradually increases with TGO growth. A family of TGO shapes, dependent on Ψ, is plotted in Fig. 4. From Eqs. (8) and (10), when the TBC is thick ($h/L \to \infty$), the stress field caused by [11] takes the form

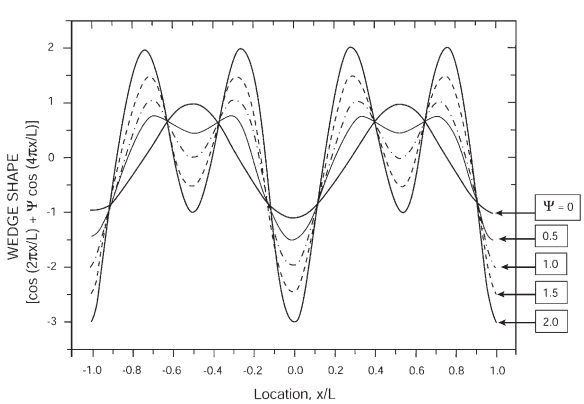

Fig. 4. A family of TGO shapes expressed by a shape factor for the TGO defined as, $\Psi \equiv U_2/U_1$.

$$\begin{cases} \sigma \equiv \sigma_{yy} = \dfrac{EU_1\pi}{L(1-\nu^2)}\left(\Sigma_1 \cos\dfrac{2\pi x}{L} + \Sigma_2\Psi \cos\dfrac{4\pi x}{L}\right), \\ \tau \equiv \sigma_{xy} = \dfrac{EU_1\pi^2}{L(1-\nu^2)}\left(\Theta_1 \sin\dfrac{2\pi x}{L} + \Theta_2\Psi \sin\dfrac{4\pi x}{L}\right), \end{cases} \tag{12}$$

where the dimensionless coefficients Σ, Θ depend on y/L according to

$$\begin{cases} \Sigma_1 = e^{-2\pi y/L}\dfrac{L + 2\pi y}{2L};\ \Sigma_2 = e^{-4\pi y/L}\dfrac{L + 4\pi y}{L}, \\ \Theta_1 = e^{-2\pi y/L}\dfrac{y}{L};\qquad \Theta_2 = e^{-4\pi y/L}\dfrac{4y}{L}. \end{cases} \tag{13}$$

3. Stress intensity factors and energy release rates

In order to simulate cracking and delamination of the TBC, the preceding stress field (12) must be coupled with crack patterns. Two basic situations are explored: (a) a single (isolated) crack extending from above one of the undulations; and (b) a series of identical converging cracks that coalesce to form a dominant crack much larger than the wavelength. For the isolated crack, there is symmetry about $x = 0$. For the periodic array the stresses are symmetric about the vertical plane through each crack midpoint and the midpoint of each ligament between the cracks. Linear elastic mechanics dictates that the normalized mode I and mode II stress intensity factors be expressed as functions of crack length, a/L, and crack location, y/L, as:

$$\begin{cases} \dfrac{K_I L(1-\nu^2)}{EU_1\sqrt{\pi a}} = f_I\left(\dfrac{a}{L},\dfrac{y}{L},\Psi\right), \\ \dfrac{K_{II} L(1-\nu^2)}{EU_1\sqrt{\pi a}} = f_{II}\left(\dfrac{a}{L},\dfrac{y}{L},\Psi\right). \end{cases} \tag{14}$$

The corresponding energy release rate is, $G = (1-\nu^2)(K_I^2 + K_{II}^2)/E$. Note that the stress intensity factors also depend on the normalized TBC thickness, h/L. The crack faces are assumed frictionless, such that contact produces only normal pressure acting on the faces. Friction is introduced implicitly at the end of the analysis when the energy release rate is equated to the (mode II) toughness of the TBC.

Planes of crack extension parallel to the interface are of practical interest (Fig. 2). While the crack is subject to mixed mode, it will become apparent that the sign of K_{II} is such that the crack always attempts to divert *toward the TGO* [29]. As it approaches, it encounters dense material having higher toughness [4]. Accordingly, the crack continues to extend parallel to the interface, within the TBC (Fig. 2). In some instances, the toughness gradient is such that the crack can penetrate the dense layer, extend through the TGO to the bond coat, and continue along this interface.

4. An isolated crack in a thick TBC

Even though the finding is that the isolated crack is not able to break through the regions of compression on either sides of the crack, the situation will be briefly reviewed for completeness. The stress intensity factors K_I and K_{II} can be calculated by applying the tractions [12] to the faces of the crack, with due account for modification of the normal traction if contact occurs. When the TBC thickness is infinite, K_I is strictly a function of σ, independent of τ, and K_{II} is function only of τ. Assuming no contact occurs, the intensity factors can be obtained by integrating the relevant Green's function [23] giving

$$\begin{cases} \dfrac{K_I L(1-\nu^2)}{EU_1\sqrt{\pi a}} = \dfrac{1}{a}\displaystyle\int_{-a}^{a}\sqrt{\dfrac{a+s}{a-s}}\left(\Sigma_1 \cos\dfrac{2\pi s}{L} + \Sigma_2\Psi \cos\dfrac{4\pi s}{L}\right) ds, \\ \dfrac{K_{II} L(1-\nu^2)}{EU_1\sqrt{\pi a}} = \dfrac{\pi}{a}\displaystyle\int_{-a}^{a}\sqrt{\dfrac{a+s}{a-s}}\left(\Theta_1 \sin\dfrac{2\pi s}{L} + \Theta_2\Psi \sin\dfrac{4\pi s}{L}\right) ds. \end{cases} \tag{15}$$

The mode II intensity factor is not altered by contact, but the mode I factor is significantly affected by contact, as will be discussed in Section 5.

Results obtained by numerical integration are

shown in Fig. 5(a)for the case, $\Psi = 0$. The first of Eq. (15) reveals that the normalized mode I stress intensity $K_I L(1-\nu^2)/EU_1\sqrt{\pi a}$ decreases with increasing crack length, reaching zero at $a/L = 0.38$. It becomes negative thereafter, indicating that the crack faces are closed near the tip and experience compression. When the crack tip is closed and contact is taken into account, the mode I solution in Eq. (15) is no longer valid. However, as long as the frictional forces between the faces are ignored, the results presented for K_{II} in Eq. (15) are still applicable, since the normal traction at the contact has no effect on K_{II} for the infinitely thick layer. The normalized mode II stress intensity initially increases, reaches a maximum, vanishes at $a/L = 0.61$ and changes sign for longer cracks.

Using a procedure similar to that discussed in Section 5 for the periodic cracks, a solution for the mode I stress intensity factor has been computed accounting for crack face contact. Then, $G = (1-\nu^2)(K_I^2 + K_{II}^2)/E$ is computed as a function of crack length for all realistic shape factors. It is found that there is always a value of a/L at which G becomes zero. That is, while an isolated crack may initiate and grow in the TBC in a region of tension above an undulation, inevitably the crack becomes trapped within the regions of compression lying on either side of the initiation site.

5. A periodic array of collinear cracks

For a periodic array of collinear cracks subjected to normal traction σ (cf. Eq. (12)) on the crack faces, the mode I stress intensity factor can be obtained by integrating Green's function [23] to obtain the following closed form expression, which is valid when crack face contact is ignored:

$$\frac{K_I L(1-\nu^2)}{EU_1\sqrt{\pi a}} = \sqrt{\frac{\pi L}{2a}}\cos\frac{\pi a}{L}\sqrt{\sin\frac{2\pi a}{L}}\Big[\Sigma_1 \qquad (16)$$

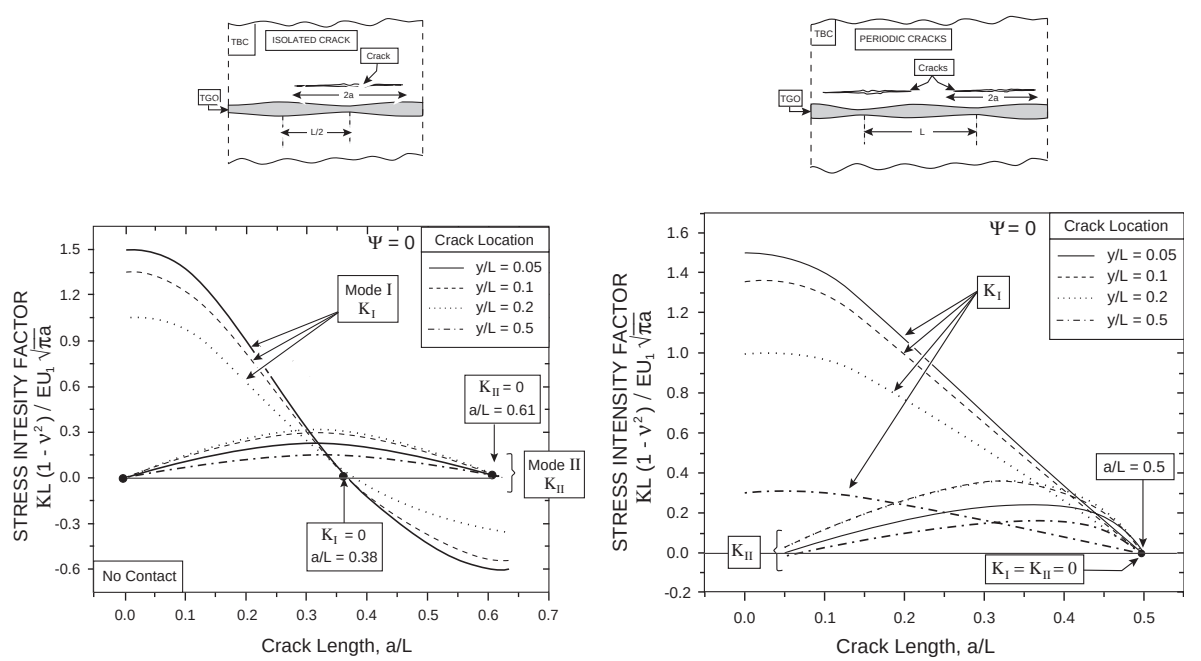

Fig. 5. (a) Normalized mode I and II stress intensity factors plotted as a function of crack length a/L for an isolated crack located above one of the undulations with $\Psi = 0$. The TBC thickness is infinite and the elastic properties are homogeneous. Contact between the crack faces is ignored. (b) Normalized mode I and II stress intensity factors, plotted as a function of crack length a/L for a periodic array of cracks with $\Psi = 0$. The TBC thickness is infinite and the elastic properties are homogeneous. The TGO undulation wavelength is L. Contact between the crack faces does not occur.

$$+ \Sigma_2\Psi\left(1-3\sin^2\frac{\pi a}{L}\right)\Bigg].$$

The corresponding Green's function for mode II does not appear to exist in the literature. However, the problem can be solved in closed form by using complex variable methods (as outlined in Appendix A) giving

$$\frac{K_{II}L(1-\nu^2)}{EU_1\sqrt{\pi a}} = \pi\sqrt{\frac{\pi L}{2a}}\sqrt{\sin\frac{2\pi a}{L}}\Bigg[\Theta_1\sin\frac{\pi a}{L} + \Theta_2\Psi\left(-\frac{1}{4}\sin\frac{\pi a}{L} + \frac{3}{4}\sin\frac{3\pi a}{L}\right)\Bigg]. \quad (17)$$

This solution is valid when contact of the crack faces occurs, as long as there is no friction.

Plots of the normalized stress intensity factors for periodic collinear cracks are given in Fig. 5(b) for the case where $\Psi = 0$, as determined from Eqs. (16) and (17). For this shape factor, no contact occurs, and both K_I and K_{II} are non-negative for all crack lengths. *However, they both vanish when the cracks converge at* $a/L = 1/2$. Note that K_I approaches zero as $(a/L-1/2)^{3/2}$, while K_{II} is relatively larger near $a/L = 1/2$, approaching zero in proportion to $(a/L-1/2)^{1/2}$. Thus, the cracks will arrest with a small remaining ligament at a crack length where $G = (1-\nu^2)(K_I^2 + K_{II}^2)/E$ falls below the toughness Γ_{tbc} at the relevant mode mixity. Moreover, if crack face contact is ignored, K_I and K_{II} each become zero for any Ψ as the cracks converge, as can be seen from Eqs. (16) and (17). Indeed, if crack face contact is ignored, any equilibrated stress distribution having the same period as the cracks will lead to zero K_I and K_{II} as the cracks converge. Consequently, ligaments between the cracks persist regardless of the TGO thickness variation.

The key to crack coalescence is crack face contact, which occurs when Ψ is sufficiently large. Two scenarios have practical relevance.

(i) Scenario I: The TGO grows such that both U_1 and U_2 increase in proportion, with fixed shape factor $\Psi > 0$. The advancing tip must pass through a zone of pure mode II, with the tip closed, until contact wedges the tip open and mode I conditions resume in final ligament failure.
(ii) Scenario II: The initial stages of the TGO growth occur under conditions dominated by U_1, with $\Psi \approx 0$. The cracks advance according to the results in Eqs. (16) and (17) (Fig. 5) until they arrest, prior to coalescence, where they are subject to dominant mode II, but with the tip still slightly open. Further growth of the TGO is envisaged to cause *both* U_1 *and* Ψ *to increase*, until contact occurs behind the tip, whereupon the ensuing wedging drives the now dominantly mode I cracks across the remaining ligaments.

Both scenarios require a reformulated solution to account for contact, which occurs if Eq. (16) indicates negative K_I. In accordance with Eq. (16), K_I becomes negative for a crack half-length, a_0/L, governed by the magnitude of a mode I shape coefficient, $\alpha_\sigma \equiv (\Sigma_2/\Sigma_1)\Psi$, such that

$$\frac{a_0}{L} = \frac{1}{2}, \quad \alpha_\sigma < \frac{1}{2}, \qquad \frac{a_0}{L} = \frac{1}{\pi}\sin^{-1}\sqrt{\frac{1}{3} + \frac{1}{3\alpha_\sigma}}, \quad \alpha_\sigma > \frac{1}{2} \quad (18)$$

as plotted in Fig. 6(a). Note that α_σ combines the dependence on the crack position y/L above the interface and the undulation shape. Contact is associated with $\alpha_\sigma > 1/2$. scenario I pertains if $\alpha_\sigma > 1/2$ in the early stages of the cracking process, while scenario II governs if most of the crack advance occurs with $\alpha_\sigma < 1/2$. In both scenarios, the condition $\alpha_\sigma > 1/2$ must be met at some stage in the cracking process.

5.1. Solution procedure for mode I contact

If $\alpha_\sigma > 1/2$ and $a > a_0$, two possibilities define the scope of the analysis.

(i) The mode I stress intensity, satisfies $K_I = 0$, with crack face contact occurring over a zone that extends up to the tip.
(ii) The mode I stress intensity, satisfies $K_I = 0$, with a contact zone forming behind the tip, whereupon the compressive force at the contact wedges open the tip.

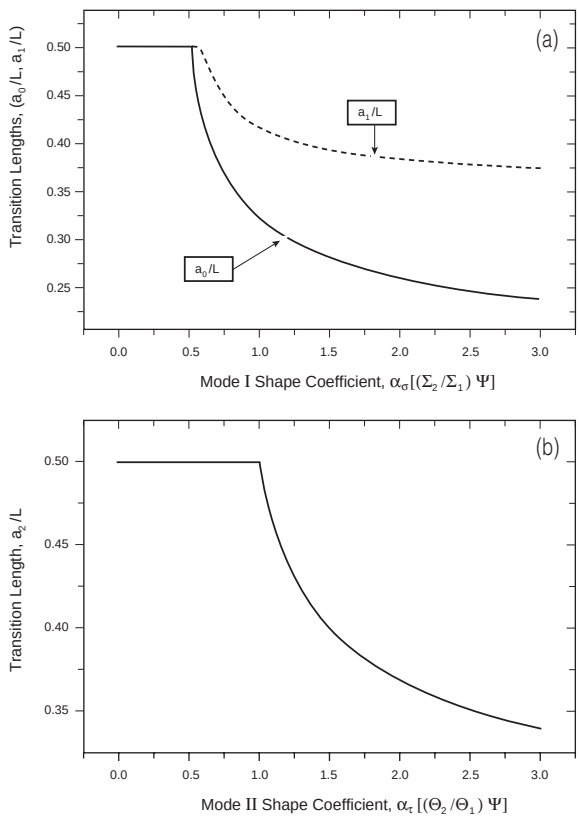

Fig. 6. (a) Transition values of the crack lengths a_0 and a_1 where the crack tip first closes and reopens, respectively. (b) Transition values of the crack length a_2 where the mode II stress intensity factor vanishes.

In either case, the contact area and contact pressure must be solved. A distributed force method is adopted. The crack surface ($0 \le x \le a$) is equally divided into $N-1$ elements with N nodes. The coordinate of node j is $x_j = (j-1)a/(N-1)$. For $1 \le i, j \le N$, let M_{ji} be the crack opening displacement at node j caused by a pair of normal unit concentrated loads of opposite signs acting on the crack faces at node i. From the solution of the crack opening profile of collinear cracks [23],

$$M_{ji} = \begin{cases} \dfrac{4(1-\nu^2)}{\pi E}\tanh^{-1}\sqrt{\dfrac{1-(\cos(\pi a/L)/\cos(\pi x_i/L))^2}{1-(\cos(\pi a/L)/\cos(\pi x_j/L))^2}}; & j \le i, \\ \dfrac{4(1-\nu^2)}{\pi E}\coth^{-1}\sqrt{\dfrac{1-(\cos(\pi a/L)/\cos(\pi x_i/L))^2}{1-(\cos(\pi a/L)/(\cos(\pi x_j/L))^2}}; & i < j \le N. \end{cases} \tag{19}$$

M_{ji} is logarithmically singular when $i = j$, and, therefore, M_{ii} is taken to be the average of the displacement field over a region of width that is small compared to the element width and centered on node i. An arbitrary distribution of normal traction on the faces can be simplified by a series of concentrated loads F_i ($i = 1 \sim N$) acting on the nodes. The resulting displacement field is then characterized by

$$\delta_j = \sum_{i=1}^{N} M_{ji}F_i \quad (j = 1 \sim N). \tag{20}$$

Denote the first and last node of the contact area by m and n, respectively. The crack tip is open if $n < N$. Inside the contact area ($m \le k \le n$), the traction F_k (which is a combination of the sinusoidal wedge stress load (σ in Eq. (12)) and contact pressure) is unknown, but the displacement satisfies $\delta_k = 0$. Outside the contact area, the crack face openings δ_l are unknown (but positive), whereas the traction is obtained from σ in Eq. (12). The total number of unknown forces and opening displacements is N, which is equal to the number of equations. The iteration procedure is as follows.

(a) Make an initial guess of m and n.
(b) Solve Eq. (20) to obtain the F_k in the contact zone and δ_l outside that zone.
(c) The solution of the problem is found when (i) the contact forces F_k are positive within the contact zone, and (ii) the crack faces are open ($\delta_l > 0$) outside the contact zone. Otherwise, adjust m and n, and go to (b) to start another iteration.

When the iteration has converged, if $n < N$, K_{I} is obtained by superposition of the stress intensities caused by the individual F_k. Numerical results have been computed using 500 elements. Numerical experiments to solve a similar contact problem for an isolated crack where an analytical solution [23] was available demonstrated that this force method is highly accurate.

5.2. Fixed shape factor: scenario I

The problem just described provides a solution for $K_{\mathrm{I}}L(1-\nu^2)/(EU_1\sqrt{\pi a})$ when $\alpha_\sigma > 1/2$, as a

function of a/L and α_σ (when $\alpha_\sigma < 1/2$, Eq. (16) applies). The normalized half-crack length, a_1/L, at which the tip reopens is a function of α_σ, and its dependence is plotted in Fig. 6(a) along with the half-crack length, a_0, at which the tip first closes. At $a = a_0$, K_{II} is positive. The crack half-length, a_2, at which K_{II} becomes zero is important in determining the condition for crack coalescence in scenario I. It depends on a mode II shape coefficient, $\alpha_\tau \equiv (\Theta_2/\Theta_1)\Psi$, such that, by Eq. (17):

$$\frac{a_2}{L} = \frac{1}{2}, \qquad \alpha_\tau < 1,$$
$$\frac{a_2}{L} = \frac{1}{\pi}\sin^{-1}\sqrt{\frac{2}{3} + \frac{1}{3\alpha_\tau}}, \qquad \alpha_\tau > 1 \tag{21}$$

plotted in Fig. 6(b).

As the crack length increases above a_0, (i) pertains and the tip is closed. But at length, a_1, the tip reopens and (ii) holds. If the tip reopens before K_{II} reaches zero, $a_0 < a_1 < a_2$, the energy release rate G remains positive at all crack lengths, including at coalescence. Then, there is a minimum energy release rate, G_{min}, that occurs at $a = a_1$. If G_{min} is larger than the relevant toughness, the collinear cracks propagate across the ligaments to coalescence.

However, if K_{II} reaches zero while the crack tip is still closed ($a_0 < a_2 < a_1$), then, $G = 0$ at $a = a_2$, and the crack necessarily arrests at $a < a_2$. Therefore, the crack length at which the crack tip reopens, a_1, is critical. The combinations $(y/L,\Psi)$ that enable coalescence ($a_0 < a_1 < a_2$) reside within the shaded domain of Fig. 7. Outside that domain, $G_{min} = 0$, and an intact ligament always remains (unless an external load is imposed).

Two illustrations showing the evolution of K_I and K_{II} with crack length a/L are plotted in Fig. 8. In Fig. 8(a), where $a_0 < a_1 < a_2$, the combination $y/L = 0.15$ and $\Psi = 0.6$ resides in the shaded domain of Fig. 7. For this case, $a_0/L = 0.36$, $a_1/L = 0.44$ and $a_2/L = 0.5$. Note that, for $a > a_1$, K_I increases sharply as coalescence is approached, and that G_{min} obtains at $a = a_1$, when the crack reopens. In fact, $K_I \to \infty$ as the ligament length $l = L - a \to 0$ because material has been selectively inserted in the regions of contact, wedging open the crack tips. The associated mathematical statement is that, at small l, the load sustained by each ligament scales as $\sim 1/\ln(L/l)$, such that $K_I \sim 1/\sqrt{l}\,\ln(L/l)$. Accordingly, $K_I \to \infty$ as $l \to 0$. In the counter-example (Fig. 8(b)), with $a_0 < a_2 < a_1$ both K_I and K_{II} are zero at $a = a_2$.

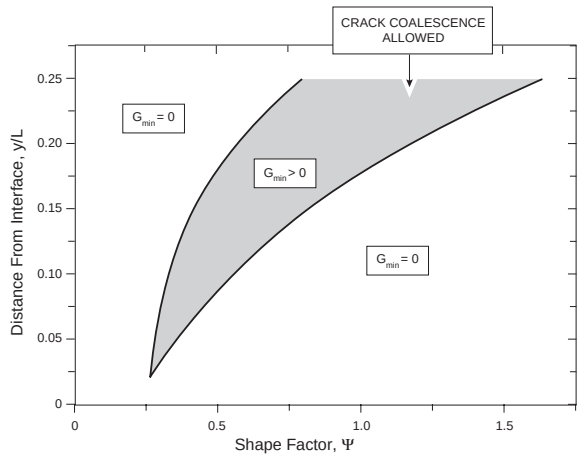

Fig. 7. Mechanism domains in crack location (y/L)/undulation shape (Ψ) space. The shaded domain represents the regime $a_0 < a_1 < a_2$ wherein the energy release rate is finite for all crack lengths in scenario I.

Since the minimum is attained at $a = a_1$ (Fig. 8(a)), where $K_I = 0$, the energy release rate becomes, $G_{min} = (1-\nu^2)K_{II}^2/E$, with K_{II} evaluated using Eq. (17). Normalized values, $G_{min}(1-\nu^2)L/(EU_1^2)$, are non-zero only in the range of $(y/L,\Psi)$ shown in Fig. 9, consistent with the condition, $a_0 < a_1 < a_2$ (Fig. 7). For $0.15 \le y/L \le 0.2$ and $0.5 \le \Psi \le 1$, $G_{min}(1-\nu^2)L/(EU_1^2)$ falls in the range 0.0005–0.002. Specifically, $G_{min}(1-\nu^2)L/(EU_1^2) = 0.0013$ for $\Psi = 0.6$ when $y/L = 0.15$, corresponding to the location of the plane in the uncracked TBC on which the shear stress is the greatest.

Inserting some typical numbers for an EB-PVD system [9] assesses the utility of these results. A more complete assessment is provided below, by means of a full, cyclic simulation conducted using a finite element methodology. Experiments and cyclic models indicate that the TGO displacement increases on a cycle-by-cycle basis [8,15,20,28]. After many cycles, representative of those experienced in practice, the displacements are of order, $U_1 \approx 5$ μm (Fig. 2), while the wavelength of the undulations is, $L \approx 30$ μm (Fig. 2). The TBC is

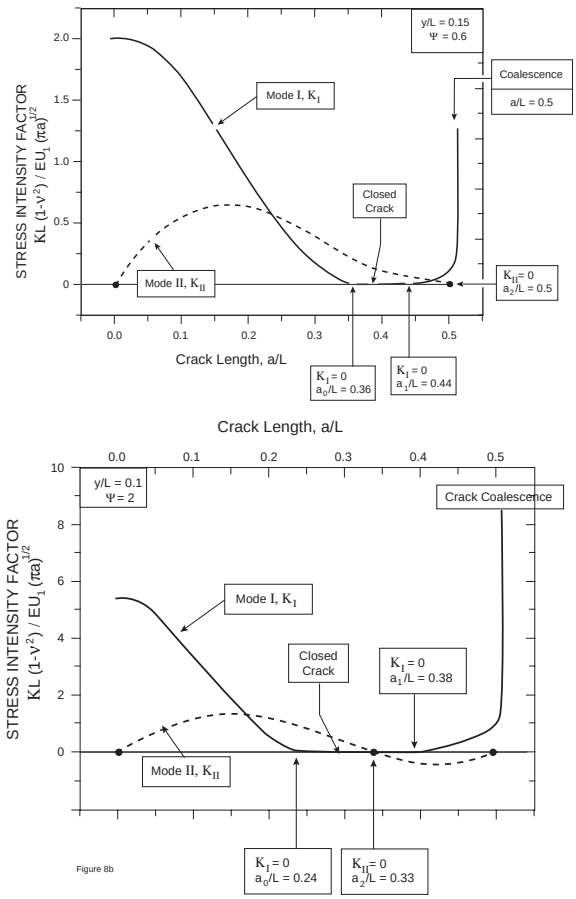

Fig. 8. (a) Stress intensity factors for a case with $a_0 < a_1 < a_2$ such that the energy release rate is finite for all crack lengths. The minimum G_{min} occurs for $a = a_1$. (b) Stress intensity factors for a case with $a_0 < a_2 < a_1$ such that the energy release rate is zero at $a = a_2$ during contact.

anisotropic, with in-plane and out-of-plane modulus both lower than the modulus of the bond coat and the substrate [4]. For this assessment, an average value for the overall system has been selected ($E \approx 100$ GPa). With this choice, the minimum energy release rate (for $\Psi = 0.6$ when $y/L \cong 0.15$ is $G_{min} \approx 80$ J/m^2, similar to the mode II toughness of the TBC [4,26,28]. This consistency lends credence to the basic mechanics concepts.

For displacements in the range, $U_1 \approx 5$ μm, if there were no cracks, the stresses induced in the TBC would be huge (several GPa). Hence the inevitability of TBC cracking as well as the large

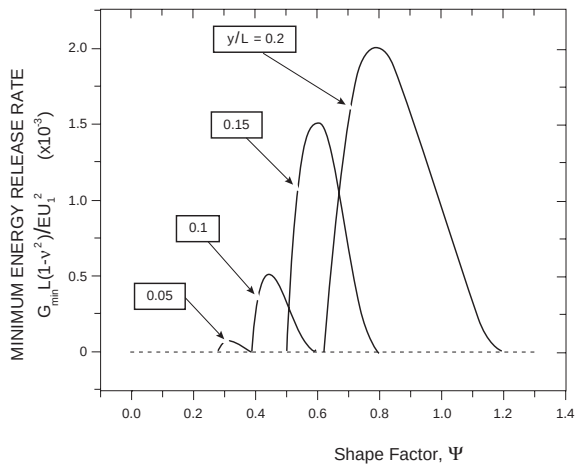

Fig. 9. Normalized minimum energy release rate for scenario I. This value is attained when the crack first reopens at $a = a_1$ for conditions wherein $a_0 < a_1 < a_2$.

crack opening displacements immediately above the initial imperfections (Fig. 2).

5.3. Variable shape factor: scenario II

Here it is imagined that the periodic cracks form and extend under conditions dominated by the U_1 component of TGO growth, such that the TBC remains attached by relatively small ligaments. With further growth of the TGO, it is surmised that the U_2 component becomes more prominent, such that Ψ increases until contact and wedging occur behind the crack tip. In this scenario, the tip is never fully closed. Results for the normalized energy release rate for cracks with $a/L \geq 0.45$ are shown in Fig. 10, for $y/L = 0.15$ and various Ψ. The dashed lines apply to cases wherein $\alpha_\sigma < 1/2$, such that no contact occurs, whereupon Eqs. (16) and (17) are valid. Such cracks necessarily arrest prior to coalescence as already discussed. When $\Psi \geq 0.6$, (the solid curves in Fig. 10), contact occurs causing an abrupt increase in energy release rate with further crack advance. The wedging action produces crack tip conditions that are dominantly mode I. The cracks become unstable and dynamically coalesce once the combination of U_1 and U_2 cause G to attain the relevant TBC toughness.

In this scenario, cracks are susceptible to

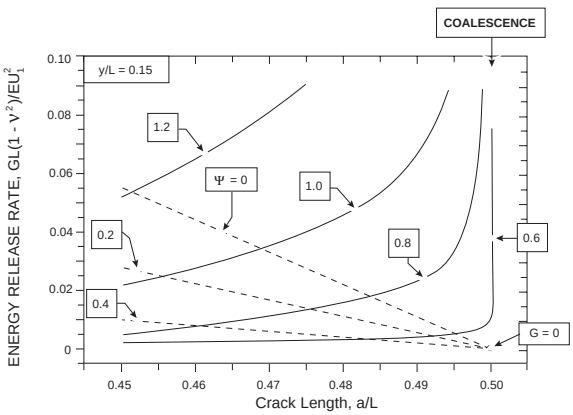

Fig. 10. Normalized energy release rate as a function of crack length during the final stage of ligament fracture for scenario II. No contact occurs for the cases with dashed lines and the cracks arrest because G becomes zero. For the solid curves, contact occurs well behind the crack tip, causing G to increase with increase in crack length once the contact has formed.

coalescence at U_1 significantly smaller than in the previous scenario, with a consequent reduction in the TBC durability. The realization emerges in the full-scale numerical simulations described in the following section.

6. Application to TBC failure

When the TBC thickness is finite, the normal and shear stress components cannot be decoupled and there is no analog of the preceding analysis. Instead, finite element analysis has been used, inspired by the basic mechanics concepts outlined above. The details are described elsewhere [28]. The basic idea is that a system with an initial imperfection is subjected to temperature cycling to simulate operating condition. In the calculations, growth of the TGO is imposed during the high temperature segment of the cycle. Plastic deformation of the bond coat occurs upon cooling and reheating, and the TGO deforms plastically at the high temperature [12]. The consequence of these deformations, which occur during each cycle, is a shape distortion of the TGO, that increases on a cycle-by-cycle basis [8,12]. This distortion induces stresses and cracking in the TBC, analogous to the wedge displacements used in the present model. In the FEM simulation the thickness of the TGO expands uniformly, as observed for actual systems, and the lateral growth of the TGO is accommodated by the shape distortion. The shape distortion produces oscillatory stress in the TBC of the same character as those modeled by the wedging displacements used in the present study. This underlies the rationale for using the wedging displacements of the present model.

A typical outcome is visualized from the finite element mesh [25,28] presented (for $\Psi > 0$) at a stage in the crack growth where its length exceeds, a_1 (Fig. 11). Note how the TGO has displaced upward outside the imperfection and that the contact at that location has, indeed, wedged open the crack as it progresses toward coalescence. Energy release rates for this problem are presented in Fig. 12. Note the existence of the minimum prior to coalescence and of a functional dependence on crack length similar to that ascertained from Fig. 8(a). It is also apparent that, after the first few cycles, the *normalized energy release rate* is essentially invariant with additional cycling. Changes in the absolute value are attributed almost exclusively to the cyclic increase in U_1. An example of the trend in absolute values (Fig. 13) traces the increase in the minimum energy release rate with

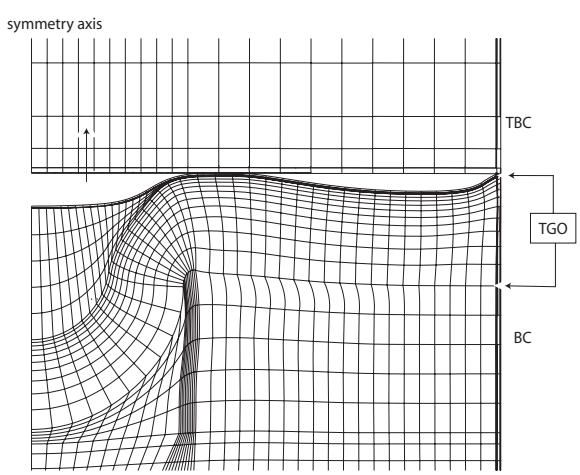

Fig. 11. A finite element mesh from a cyclic simulation showing the undulation of the TGO and the extent of cracking just prior to coalescence [28]. Note the domain of contact at the imperfection periphery, behind the crack tip, and the uplift of the TBC caused by the contact.

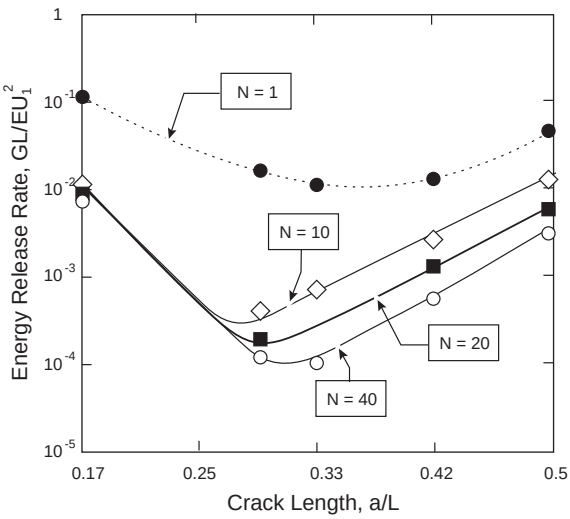

Fig. 12. Trend in the non-dimensional energy release rate as a function of crack length determined from a full cyclic simulation [28]. Note the existence of a minimum prior to coalescence. Here N is the number of thermal cycles. With this normalization, the energy release rate is essentially invariant with N, after three first few cycles.

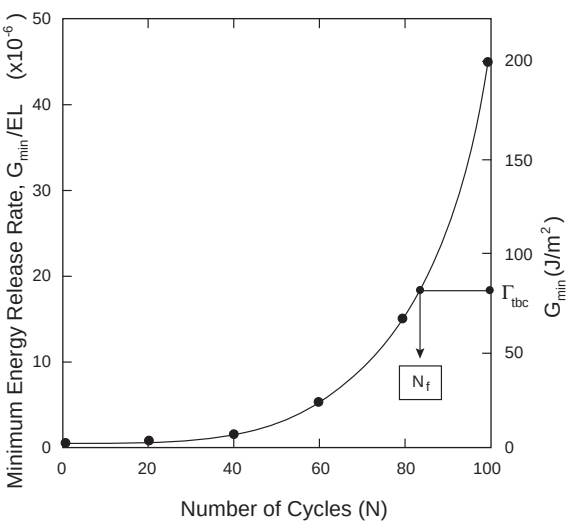

Fig. 13. The variation in the minimum energy release rate, G_{min}, with the number of cycles, N [28]. When G_{min} attains the mode II toughness of the TBC the system fails, as indicated in the figure.

the number of thermal cycles. Where this minimum crosses the mode II toughness of the TBC, Γ_{tbc}, gives the number of cycles to failure, as indicated on the figure. These predictions are consistent with experimental measurements [9].

Several connections between the simulations and the analytic results are elaborated for clarification. In the simulations and in actual experiments, the undulation shape factor, Ψ, changes. At the outset, $\Psi \approx 0$, dictated by the initial shape of the imperfection. This small value leads to the largest mode I stress intensity factor for short cracks in the TBC ($a < a_0$), encouraging nucleation and initial propagation. If this shape were to be retained throughout, the crack would arrest prior to coalescence (Figs. 5 or 10). However, as cycling proceeds, the upward displacement induced at the outer periphery of the imperfection (Fig. 11), causes Ψ to increase, indicative of scenario II above. Consequently, coalescence becomes possible and will occur when $G_{min} \rightarrow \Gamma_{tbc}$, as depicted in Fig. 13. This evolution in the undulation shape factor is a key mechanics principle underlying the occurrence of crack coalescence and failure in TBC systems.

7. Conclusion

Coatings subject to residual compression, such as TBCs, eventually fail by buckle-driven delamination [4]. Failure coincides with the coalescence of small cracks that form at geometric imperfections. The mechanics governing crack coalescence and failure are addressed in the present analysis. A model is introduced that simulates stresses induced in the TBC by imposing spatially varying displacements motivated by TGO growth and thermal cycling. Energy release rates for cracks evolving in this stress field are determined. Two different failure scenarios are explored.

(i) In the first, the TGO shape factor Ψ is nonzero and invariant. The TBC crack transits from mixed mode to pure mode II as it penetrates the zones of prior compression induced in the TBC. With further TGO growth, the crack emerges from this zone and the tip is reopened by wedging force acting across a zone

of contact behind the tip. The ensuing mode I stress intensity becomes infinite as the cracks coalesce: enabling (for a range of Ψ) a non-zero energy release rate at all crack lengths, with a minimum occurring at a characteristic crack length, a_1. Equating this minimum to the mode II toughness of the TGO gives a criterion for crack coalescence and failure.

(ii) In the second, the initial TGO shape factor ($\Psi \approx 0$) is such that a large energy release rate develops at initiation. The cracks readily extend, but must arrest with a relatively small intact ligament. The subsequent TGO growth evolves in a manner that causes the shape factor Ψ to increase, resulting in the formation of a contact zone behind the existing crack tip. Further development of the contact upon TGO growth imposes a force that wedges open the tip, increasing G up to the toughness of the TBC, causing coalescence. This scenario enables coalescence at smaller levels of normal displacement, U_1, and is expected to prevail in actual TBC systems.

Full-scale simulations inspired by these basic mechanics concepts have affirmed that the second scenario applies to thermal barrier systems of the type depicted in Fig. 2 and, moreover, that the predicted cycles to failure correlate well with experimental observations.

The coalescence of cracks on a plane subject to periodic traction has other intriguing aspects, yet to be explored. The present study has been limited to strictly two-dimensional crack growth. Conceivably, the straight crack fronts might be unstable to perturbations of shape in their plane, giving rise to a three-dimensional coalescence pattern.

Appendix A. The mode II solution for periodic cracks

Green's function for concentrated loads applied to the crack faces of the periodic cracks with the symmetry required for the mode II problem of interest in this paper has not been found in the literature. The solutions for the problem for the infinitely thick TBC ($h = \infty$) can be obtained using the complex variable method of plane elasticity. In this Appendix, the cracks are taken to lie on the plane $y = 0$. With reference to the periodic cell of Fig. 3, the boundary conditions for collinear cracks subject to sinusoidal shear loading require $\sigma_{yy} = 0$ everywhere along the plane of the cracks, $u_x = 0$ on the ligaments between the cracks, and $\sigma_{xy} = \tau_0(x)$ on the crack faces. Specific results will presented for $\tau_0 = \tau_1^* \sin(2\pi x/L)$ and $\tau_0 = \tau_2^* \sin(4\pi x/L)$ where $\tau_1^* = \pi^2 E U_1 \Theta_1/[L(1-\nu^2)]$ and $\tau_2^* = \pi^2 E U_1 \Theta_2/[L(1-\nu^2)]$, but the general result applies to any distribution that is self-equilibrated in the sense that $\int_0^{L/2} \tau_0(x)\, \mathrm{d}x = 0$.

Solutions to plane elasticity are can be represented by functions φ and ψ, which are analytical functions of the complex variable, $z = x + \mathrm{i}y$ [24]:

$$\begin{cases} \sigma_{xx} + \sigma_{yy} = 2(\varphi' + \overline{\varphi'}), \\ \sigma_{yy} - \sigma_{xx} + 2\mathrm{i}\sigma_{xy} = 2(\bar{z}\varphi'' + \psi'), \\ 2\mu(u_x + \mathrm{i}u_y) = \kappa\varphi - z\overline{\varphi'} - \overline{\psi}, \end{cases} \tag{A1}$$

where $\mu = E/(2(1+\nu))$ and $\kappa = E/(3(1-2\nu))$. The condition that σ_{yy} vanishes along the real axis provides $\psi = -z\varphi' - \varphi$. Following a procedure similar to that laid out by Koiter [27] for mode I problems, one can show that the solution is

$$\varphi'(z) = \mathrm{i}\omega(z)/\chi(z), \tag{A2}$$

where

$$\chi(z) = \sqrt{\cos\frac{2\pi a}{L} - \cos\frac{2\pi z}{L}}, \tag{A3}$$

$$\omega(z) = \sum_{k=1}^{\infty} \frac{1}{4\pi} \int_{\Gamma_k} \frac{\lambda(\xi)}{\xi - z}\, \mathrm{d}\xi, \tag{A4}$$

$$\lambda(\xi) = \frac{\tau_0(\xi)}{2\mathrm{i}} \sqrt{\cos\frac{2\pi\xi}{L} - \cos\frac{2\pi a}{L}}. \tag{A5}$$

In Eq. (A4), Γ_k is a contour surrounding the kth crack. Contour integration of Eq. (A4) for the two sinusoidal components of the shear stress distribution noted above leads to

$$\omega(z) = -\frac{\tau_1^*}{2}\chi(z)\sin\frac{2\pi z}{L} - \frac{\tau_1^*}{2\sqrt{2}}\left(\cos\frac{3\pi z}{L} - \cos\frac{\pi z}{L}\cos\frac{2\pi a}{L}\right), \quad \text{(A6)}$$

$$\omega(z) = -\frac{\tau_2^*}{2}\chi(z)\sin\frac{4\pi z}{L} - \frac{\tau_2^*}{2\sqrt{2}}\left(\cos\frac{5\pi z}{L} - \cos\frac{3\pi z}{L}\cos\frac{2\pi a}{L} + \frac{1}{2}\cos\frac{\pi z}{L}\sin^2\frac{2\pi a}{L}\right). \quad \text{(A7)}$$

The mode II stress intensity factor is

$$K_{II} = \lim_{r\to 0}\sigma_{xy}\sqrt{2\pi r} = \lim_{r\to 0} -2\sqrt{2\pi r}\,\mathrm{Im}[\varphi'] \quad \text{(A8)}$$

such that for the two components

$$K_{II} = \tau_1^*\sin\frac{\pi a}{L}\sqrt{\frac{L}{2}\sin\frac{2\pi a}{L}}, \quad \text{(A9)}$$

$$K_{II} = \tau_2^*\sqrt{\frac{L}{2}\sin\frac{2\pi a}{L}}\left(-\frac{1}{4}\sin\frac{\pi a}{L} + \frac{3}{4}\sin\frac{3\pi a}{L}\right). \quad \text{(A10)}$$

References

[1] Miller RA. J Am Ceram Soc 1984;67:517.
[2] Hillery RV, editor. NRC Report. Coatings for high-temperature structural materials. Washington, DC: National Academy Press; 1996.
[3] Miller RA. Proceedings of the Thermal Barrier Coatings Workshop, NASA CP, 3312; 1995.
[4] Evans AG, Mumm DR, Hutchinson JW, Meier GH, Pettit FS. Prog Mater Sci 2001;46:505.
[5] Stiger MJ, Yanar NM, Topping MG, Pettit FS, Meier GH. Z Metallkd 1999;90:1069.
[6] Padture NP, Gell MEH, Jordan EH. Science 2002;296:280.
[7] Rabiei A, Evans AG. Acta mater 2000;48:3963.
[8] Karlsson AM, Evans AG. Acta mater 2001;49:1793.
[9] Mumm DR, Evans AG, Spitsberg IT. Acta mater 2001;49:2329.
[10] Tolpygo VK, Clarke DR. Acta mater 2000;48:3283.
[11] Ruud JA, Bartz A, Borom MP, Johnson CA. J Am Ceram Soc 2001;84:1545.
[12] Karlsson AM, Hutchinson JW, Evans AG. J Mech Phys Solids 2002;50:1565.
[13] Spitsberg IT, Mumm DR, Evans AG. J Mater Res, in press.
[14] Gell M, Vaidyanathan K, Barber B, Cheng J, Jordan EH. Metall Mater Trans 1999;30A:427.
[15] He MY, Hutchinson JW, Evans AG. Mater Sci Eng A 2003;345:172–8.
[16] Busso EP, Lin J, Sakurai S, Nakayama M. Acta mater 2001;49:1515.
[17] Busso EP, Lin J, Sakurai S. Acta mater 2001;49:1529.
[18] Vaβen R, Kerkhoff G, Stover D. Mater Sci Eng A 2001;303:100.
[19] Tzimas E, Mullejans H, Peteves SD, Bressers J, Stamm W. Acta mater 2000;48:4699.
[20] Evans AG, Hutchinson JW, He MY. Acta mater 1999;47:1513.
[21] Evans AG, He MY, Hutchinson JW. Acta mater 1997;45:3543.
[22] Timoshenko SP, Goodier JN. Theory of elasticity. New York: McGraw-Hill, 1969.
[23] Tada H, Paris PC, Irwin GR. The stress analysis of cracks handbook. New York: ASME Press, 2000.
[24] Muskhelishvili NI. Some basic problems of the mathematical theory of elasticity. Leiden: Noordhoff, 1953.
[25] Hibbit, Karlsson & Sorensen Inc. ABAQUS version 5.7 user's manual. Pawtucket (RI): Hibbit, Karlsson & Sorensen Inc., 1998.
[26] Vasinonta A, Beuth JL. Eng Fract Mech 2001;68:843.
[27] Koiter WT. Ing Arch 1959;28:168.
[28] Xu T, He MY, Evans AG, in press.
[29] Hutchinson JW, Suo Z. Adv Appl Mech 1992;29:63.